Received 00th January 20xx,

DOI:

Simple bottom-up synthesis of bismuthene nanostructures with suitable morphology for competitive performance in electrocatalytic nitrogen reduction reaction

Stefanos Mourdikoudis,* Nikolas Antonatos, Vlastimil Mazánek, Ivo Marek, Zdeněk Sofer,*

Abstract: Nitrogen reduction to ammonia under ambient conditions has received important attention, in which highly performing catalysts are sought. A new, facile, seedless solvothermal method based on a high-temperature reduction route has been developed in this work for the production of bismuthene nanostructures with excellent performance in electrocatalytic nitrogen reduction reaction (NRR). Different reaction conditions were tested, such as type of solvent, surfactant, reducing agent, reaction temperature and time as well as bismuth precursor source, resulting in distinct particle morphologies. Two-dimensional sheet-like structures and small particles displayed very high electrocatalytic activity, attributed to the abundance of tips, edges and high surface area. NRR experiments resulted in ammonia yield of 571 ± 0.1 $\mu g h^{-1} cm^{-2}$ with a respective Faradaic efficiency of 7.94 ± 0.2 % vs Ag/AgCl. The easy implementation of the synthetic reaction to produce Bi nanostructures alloys its potential scale up to larger production yields.

Introduction

Nanostructured 2D materials often display quite different properties in comparison to their bulk counterparts. Improved mechanical, conductive and catalytic properties may arise.[1] The constant increase of the global population and of the associated energy demand require to adopt carefully designed measures for the sustainable development of mankind. Materials which can efficiently harvest, store and transport the renewable energy without producing greenhouse gas are constantly pursued. Ammonia, with a high hydrogen content (17.7 wt%), high gravimetric energy density (3 $kWh.KH^{-1}$) and straightforward operation is one of the most environmentally benign candidate materials for use as energy carriers. NH_3 is massively produced by the so-called Haber-Bosch process, which needs high temperature and pressure, while it also mostly relies on fossil fuels, being responsible for ~ 1 % of the worldwide greenhouse gas emission per year.[2] For this reason, greener, more sustainable and highly efficient routes to produce ammonia are increasingly looked for. Up to now, biological, photocatalytic and electrocatalytic methods have been studied to synthesize NH_3. Among these routes, electrocatalytic nitrogen reduction reaction (NRR) has emerged as a promising technonogy. Attractive features of this reaction include mild operation conditions, water as hydrogen source and no carbon dioxide emission. Nevertheless, electrocatalytic NRR is still far from its widespread practical application, since most of the used electrocatalysts to date for this reaction display low ammonia yield and current efficiency. The extremely high stability of dinitrogen and competitive hydrogen evolution reaction (HER) are largely responsible for the above. As a consequence, developing high-efficiency NRR electrocatalytic and catalytic systems is of utmost importance for future industrial production of ammonia at ambient conditions.[3]

It is widely known that decreasing the size of at least one dimension of electrocatalysts to a few nm and producing morphologies with edges, corner and tips is one efficient strategy to generate numerous catalytically active sites. Recently, metal oxides have been widely explored for the electrochemical NRR, such as Fe_2O_3, TiO_2, InO_2, NbO_2, SnO_2 etc. For example, nanoscale maghemite electrocatalysts have been reported to reach a Faradaic efficiency of 1.9% and a weight-normalized activity of 12.5 $mol.h^{-1}mg^{-1}$ at 0.0 V_{RHE}.[4,5] Zr^{4+}-doped anatase TiO_2 displayed excellent electrochemical NRR activity with an ammonia production rate of 8.9 $\mu g h^{-1} cm^{-2}$ and a FE of 17.3 at –0.45 V vs RHE in aqueous medium at ambient conditions.[6] Apart from metal oxides, other materials such as metal chalcogenides, carbon, C_3N_4 and single-atoms catalysts have also been reported to act in a suitable way for the NRR.[6]

Bi is an interesting eco-friendly, cost-effective, easy to synthesize material, which is deemed as a promising electrode agent. It is a semimetal which displays a highly anisotropic Fermi surface, low carrier density, small carrier effective mass and long carrier mean free path.[7] In the nanoscale regime, bismuth can be converted from semi-metal to a semi-conductor, because of a quantum confinement effect, and this makes Bi particularly utile for optoelectronic and thermoelectric applications. Morphologies such as nanoparticles, nanowires, nanorods, nanotubes, nanoplates and others have been prepared by different approaches.[8] Among them, colloidal chemical synthesis enables the synthesis of bismuth nanostructures with tuned size and shape and with the potential of scalable production. Bismuth has already shown its utility as an efficient electrocatalyst. For example, free-standing 2D Bi monolayer (bismuthene) structures displayed a high electrocatalytic efficiency for formate ($HCOO^-$) formation from CO_2 reduction reaction, with high Faradaic efficiency, small onset overpotential and high durability.[9]

In this work, we present a facile autoclave bottom-up colloidal chemical synthesis of bismuth nanostructures with diverse morphologies through the reduction of $Bi(NO_3)_3 \cdot 5H_2O$ by hydrazine at high temperatures in the presence of suitable solvents and surfactants. A range of reaction conditions was studied, aiming to identify the best material for NRR application. Very competitive outcomes for the average yield of ammonia production and the respective Faradaic efficiency were found for some of our samples. Though the synthesis of certain samples among the ones presented herein was inspired from literature, the best-performing sample in NRR was produced using a novel synthetic protocol that we developed and present for the first time, not previously reported for pnictogen nanostructures. Regarding the NRR itself, it is worthy to

note that the degree of its practical significance has come to light relatively recently and it is not yet widely explored, as is the case for other major electrocatalytic reactions. Those include for example hydrogen evolution, oxygen reduction, oxygen evolution, CO_2 reduction, alcohol oxidation and formic acid oxidation reactions, among others. Our results are discussed based on the choice of proper combinations of solvents, ligands and temperatures which generate optimum materials for use as NRR electrocatalytic agents. Control experiments and careful characterization helped to identify and better understand the catalytic activity of the different samples. This paper underlines that less reactive main group elements such as Bi with semimetal-semiconducting features can combine relatively simple and scalable synthetic routes with a competitive activity for such types of electrocatalytic reactions. Especially a two-dimensional nanostructure morphology with a high surface area and a plethora of active sites such as edges and tips was found to promote such high electrocatalytic performance.

Results and discussion

Synthesis, structure and morphology

Top-down approaches such as sonication, liquid-phase exfoliation,[10] electroreduction,[11] sputtering,[12] electrospinning,[13] and laser ablation[14] have been used for the preparation of bismuth nanostructures with two-dimensional and other morphologies. Although such methods can sometimes generate big amounts of particles, corresponding to large scale production, they may also present some drawbacks. For example, polydisperse, not well-defined shape and the appearance of structural defects can be associated with the use of top-down routes. On the other hand, colloidal bottom-up synthesis routes, taking place in aqueous or organic medium, allow the production of well-defined, nicely tailored nanostructures with desired shapes.

In the current work we chose to use autoclaves, which enable the establishment of high temperature/high pressure conditions in either hydrothermal or solvothermal synthetic routes. The temperature in the autoclave can be raised beyond the boiling point of water in hydrothermal syntheses, while the organic solvent employed as a reaction medium in the solvothermal pathway can be heated above its corresponding boiling point too. Features such as crystalline grain size, surface chemistry and composition can be tuned by adjusting parameters such as reaction temperature and time as well as types and concentrations of solvents, surfactants, precursors and reducing agents.[15] Autoclave syntheses offer advantages such as cost-effective process, facile experimental setup, as well as high and scalable yield.[16] Instrumentation, energy and material precursors cost requirements are lower compared to other solution phase synthesis routes.[17] The synergistic effect of high temperature and pressure contributes to the acquisition of highly crystalline materials without requiring further annealing stages.[18]

Our aim to synthesize Bi nanostructures with attractive activity in the NRR was also a contributing factor for the choice of autoclave synthesis in the present work. Two-dimensional morphologies and features such as the presence of edges, sharp tips and a high surface area facilitate the achievement of a higher catalytic/electrocatalytic activity. Autoclave pathways have been often employed to prepare 2D nanostructures. At relatively high pressure, the solubility and reactivity of the precursors can be increased drastically resulting In the modification of the physiochemical properties of the solvents.[19] We employed bismuth nitrate pentahydrate as Bi source, which is a quite stable precursor in air at room temperature, thus any undesired decomposition/degradation can be easily avoided. As reducing agent we used hydrazine (N_2H_4) which is a strong, water soluble reductant and can be used in either acidic or basic media. Hydrazine is a stronger reductant in basic than in acidic media, and it permits the reaction rate modulation through pH regulation. It decomposes to N_2 during synthetic reactions toward NPs, thus providing an inert atmosphere, facilitating to retain the zerovalent state of the produced NPs, even if initially the autoclave contains some amount of oxygen from the air.[20] Hydrazine is an alternative reagent compared to the more broadly used sodium borohydride ($NaBH_4$), which is however a moisture sensitive solid that can be self-hydrolyzed, unlike hydrazine, which is a stable liquid.[21] The decomposition mode of N_2H_4 will not leave unwanted oxidation products-impurities in the course of a synthetic reaction, allowing the acquisition of compositionally pure NPs with 'clean' surface chemistry. The absence of contaminants is thus an advantage, but it also indicates the necessity to add stabilizing agents (surfactants) in order to regulate the particles growth and prevent aggregation.[20]

Therefore in this work we first attempted to produce Bi nanostructures in the presence of PSS (Poly(sodium 4-styrene-sulfonate). PSS has been shown to act effectively as a surfactant for the size and shape control of bismuth nanoparticles and nanosheets prepared by hydrothermal processes. If an aqueous reaction medium is used, PSS and water molecules will be adsorbed on the surface of Bi precursors. Afterwards the ions from the precursors will be diffused and generate particles along several directions due to the polar distinction between PSS and water, thus diverse morphologies can be expected.[22] PSS is a frequently employed polymer for the preparation of a range of nanostructures. Without this, the resulting particles would be expected to grow in an uncontrolled pattern and form large aggregates. Certainly, it is noted that the acquisition of spherical or layered morphologies depends not only on the pseudo-layered structure of metallic bismuth itself, but it can also be modified by applying even subtle changes in the reaction conditions of a given hydrothermal (or other) chemical mixture.[23]

Bismuth electrocatalysts were produced herein through autoclave approaches, aiming to compare their electrocatalytic activities for NRR and find the most suitable electrocatalyst. Initially we synthesized the sample Bi-S1 based on the protocol described by Ghazali et al.[22] aiming to produce two-dimensional, nanosheet-like morphologies. In our case, sample Bi-S1 is composed of nanostructures reaching sizes in the microscale, being either three- or two-dimensional ones (Figure 1a,b). As mentioned above, even very slight modifications at the followed protocol, often not easily spotted, could somewhat alter the features of the resulting particles prepared via colloidal chemical synthetic routes such as hydrothermal processes. XRD measurement (Figure 1d) reveals that

the structures of Bi-S1 are composed of Bi(0). The peaks at 27.1, 37.9, 39.6° etc. can be assigned to zerovalent Bi, corresponding to the ICDD pattern 00-005-0519 with rhombohedral crystal structure. Interestingly, we note that even 5 h of heating were enough to avoid the presence of any signs denoting the existence of crystalline bismuth oxide phases too, such as Bi_2O_3. The complete reduction of bismuth precursor to metallic Bi by hydrazine was achieved under the applied hydrothermal route. The sharp XRD peaks denote a high crystallinity for the produced powders, which were stored in a glovebox soon after their washing and drying, prior to any other characterizations or electrocatalytic experiments. It seems that under the experimental conditions tested, fast nucleation and growth took place, facilitated by the presence of high pressure, relatively high temperature and a fairly strong reductant such as hydrazine. Initially, Bi^{2+} cations were probably generated as a result of the dissociation of $Bi(NO_3)_3 \cdot 5H_2O$. Then the bismuth cations were reduced to Bi^0 by hydrazine. The decomposition of the latter allowed to have an elevated concentration of inert gas (nitrogen) in the autoclave, preventing the oxidation of particles at the high-temperature conditions of the reaction.[24] The relatively big size of the structures of sample Bi-S1 can be possibly ascribed to the occurrence of the Ostwald ripening effect, in which small particles are formed first and they are then dissolved and re-deposited to produce bigger particles. HRTEM images (Figure 1c) indicate the existence of different crystallographic domains in the bismuth layers. PSS is a hydrophilic chain-like polymer derived from polystyrene with SO_3^- functional groups, and it has been reported to assist the formation of 2D structures (*e.g.* in exfoliation syntheses) while it also helps to disperse and stabilize the produced nanostructures, in addition to hindering their oxidation. PSS can form micelles under vigorous stirring due to the presence of the hydrophilic SO_3H moiety and hydrophobic alkyl group: in this way it is capable to encapsulate nanomaterials and as-synthesized nuclei to form particles with controlled size. It possesses a quite strong negative charge that can provide steric hindrance and electrostatic repulsions between NPs.[25,26]

Aiming to produce smaller Bi nanostructures, which might be more suitable for the NRR, in sample Bi-S2 we followed a protocol similar to the one described by Yan and co-workers.[23] It has already been reported that the size of electrocatalysts plays a critical role in NRR activity. A smaller size of bismuth crystals might expose more active sites for NRR.[27] Indeed in Bi-S2 we notice the appearance of mostly spherical (and a few polygonal-like) particles in the size range 80-120 nm (Figure 2a-c). This result is in fair agreement with that reported in the original protocol cited above.[23] Compared to the conditions used to produce the sample Bi-S1, in sample Bi-S2 hydrazine and PSS are in relatively higher proportions than the bismuth precursor. The higher concentration of hydrazine can cause a faster nucleation event, leading to the generation of abundant nuclei within a short time, suppressing particles growth and yielding smaller NPs size.[28] At the same time, the higher ratio of PSS aims toward a better stabilization and regulation of the particle size to a more narrow range. The growth sites can be more easily blocked, and the growth species can be better stabilized with an increased proportion of surfactant. This will prevent particle growth to large sizes. Another reason for the drop in size in Bi-S2 in comparison to Bi-S1 may be the much lower concentration of precursor, in respect to the amount of solvent, which is kept fixed at 50 ml. When the concentration of the growth species (monomers) in the reaction pot is high (the case of Bi-S1), the concentration of the available monomers at the interface of the nuclei (the crystal growth front) is also high. Thus the diffusion distance for the monomers is shorter, resulting in relatively high mass transfer and an elevated growth rate. Consequently, larger particles will be generated during a given growth period. For high monomer concentrations, the nanostructures growth rate is in principle controlled by reactions on the particles' surface. When the amount of precursor gets radically decreased, the lower monomer concentration induces an increase in the diffusion constant, which as as consequence decreases the growth rate. This occurs because of a lower mass transfer in the reaction system. Hence in the case of the sample Bi-S2, the particles growth is diffusion-limited. This promotes the formation of smaller NPs under otherwise similar reaction conditions as in Bi-S1 (time, temperature).[29] The composition also for this sample is zerovalent Bi, with no traces for oxides, as shown at the corresponding XRD diffractogram in Figure 2d.

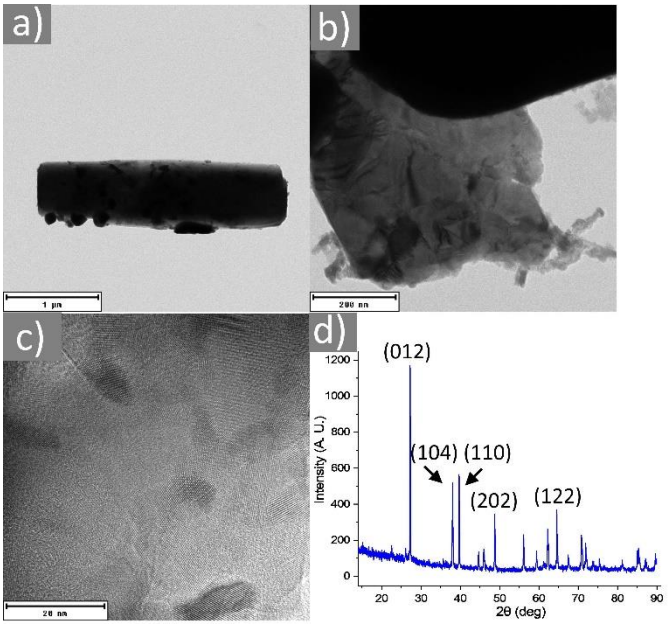

Figure 1. TEM (a), (b) and HRTEM (c) images of sample Bi-S1. XRD measurement of Bi-S1 at (d).

Though surfactants are needed for a good control of the size and shape of nanoparticles, tackling also any aggregation risks, they may deteriorate the catalytic and electrocatalytic potential of the produced materials. They may attach firmly onto the particles surface, blocking the catalytically active sites. Still, such negative effect depends also on the type of surfactant used. For instance, cationic surfactants are not suitable for catalysts with negative

charge on their surfaces.[30] We have previously shown that branched polyethyleneimine (PEI) allows noble metal nanostructures such as Pd and Au-Pt to exhibit remarkable catalytic and electrocatalytic performance respectively.[31,32] Therefore in sample Bi-S3 we kept the same conditions as in Bi-S2 with the exception of the use of PEI instead of PSS. We aimed to observe how a pnictogen element like Bi would behave with respect to its growth mode, affinity with PEI and resulting electrocatalytic properties ability, compared to the case of the above-mentioned noble metals.

Figure 2. TEM images (a-c) and XRD measurement (d) for sample Bi-S2.

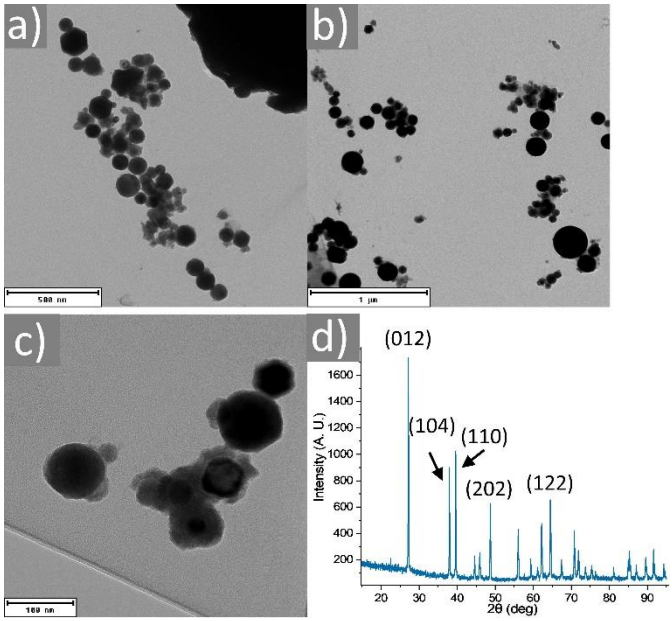

In Figure 3a-c one can notice the presence of ill-defined particles in sample Bi-S3, with size mostly below 100 nm for the majority of them. A relatively low yield was observed in terms of particles production, but the particles crystal phase was still Bi^0 (Figure 3d), as in the previous samples. Considering that hydrazine is a stronger reducing agent in basic than in acidic media, water solvent was replaced by DMF in sample Bi-S4. This aimed to boost the reducing power of N_2H_4, securing a better reaction yield. DMF is a strong base, miscible with water that can dissolve a wide range of reagents such as metallic precursors. It is a polar aprotic solvent, with wide liquid range. It displays a reducing function itself, too, and it has been suggested that the reducing capability of DMF is related to the oxidation of its aldehyde group to carboxylic group in carbamic acid, which can then decompose to CO_2 and dimethylamine at elevated temperature.[33] DMF however usually requires the presence of stabilizers during nanoparticle synthesis, as its sole use would often result in uncontrolled growth and aggregation. Still, DMF-stabilized metal NPs have been reported. Such stabilization is achieved through the interaction of amido groups of DMF with nanocrystals.[34] We have already reported the successful preparation of monodisperse Pt nanodendrites in refluxing DMF at 154 °C in the presence of branched PEI.[31,35] Therefore in sample Bi-S4 (Fig. 4a-c) the majority of the produced structures have size > 100 nm with a rather irregular morphology. This shows that the presence of hydrazine together with another element, such as Bi, instead of noble metals, can result in nanostructures with quite different morphology pattern. In what concerns the yield for Bi-S4 in terms of product mass, it was indeed higher than that of Bi-S3, thanks to the synergistic reducing effect between DMF and hydrazine.

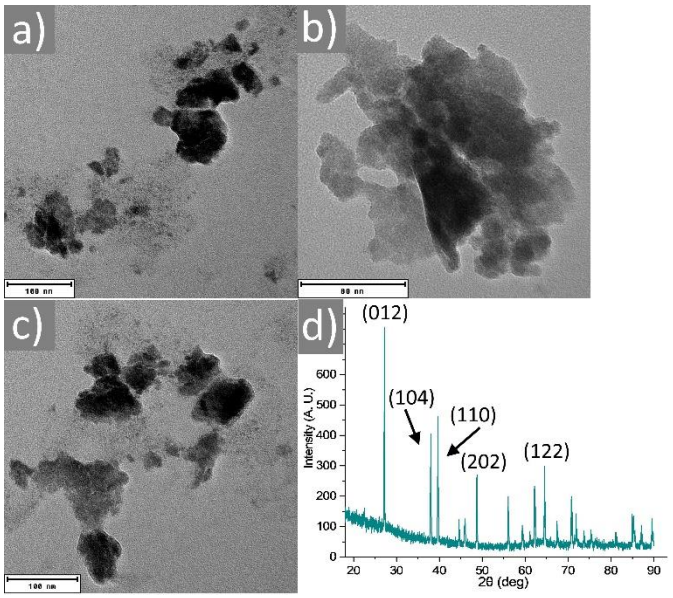

Figure 3. TEM images (a-c) and XRD measurement (d) for sample Bi-S3.

The synthesis of sample Bi-S5 was inspired by a previous work of ours on the synthesis of Pt nanoflowers, where DEG and PEI were combined.[36] Our aim was to achieve the formation of quite well-defined bismuth nanostructures with high surface area, edges and tips, facilitating a good performance toward NRR. Therefore in sample Bi-S5 we replaced DMF with DEG. In addition, a higher reaction temperature was employed (240 °C) together with a relatively shorter reaction time (1h). Apart from its reducing action, attributed mostly to its two free hydroxyl groups, DEG can also affect the resulting particle shape, acting as a capping agent.[37] It is a multidentate, high-boiling alcohol (b.p. 246 °C) which permits synthetic reactions at high temperatures even without the use of autoclaves.[38] Of course, reduction evolution in sample Bi-S5 was affected by the simultaneous presence of DEG and hydrazine. Therefore in Bi-S5 we notice the appearance of thin hexagonal plates with sizes mostly in the range 700-900 nm, together with a minority of smaller spherical particles (14.7±4.7 nm in size) on the TEM grid (Figure 5a-c). The analysis of AFM images for this sample revealed the existence of bismuthene nanosheets of 1 μm lateral size and 10 nm thickness (Figure S1a). By decreasing the scan size it became possible to locate hexagonal plates with a lateral size of a few hundreds of nanometers and a thickness range between 7-12 nm (Figure S1b). Apparently the strong heating conditions, combined with a shorter synthesis reaction helped toward the acquisition of a more homogeneous morphology pattern compared to the previous Bi samples of the current work. Apart from its XRD diffractogram

(Figure 5d), confirming its rhombohedral crystal phase, the Bi(0) composition for this sample is confirmed also by its Raman spectrum (Figure S2 at the SI). The Raman bands located at 69 and 93 cm^{-1} are attributed to the first order in-plane E_g and out-of-plane A_{1g} stretching modes of Bi-Bi bond in rhombohedral bismuth and illustrate the crystalline state of the nanostructures.[39-41] The absence of major peaks at 313 and 446 cm^{-1} denotes that there are no signs for the presence of a considerable amount of oxides such as α-Bi_2O_3.[38] The sample Bi-S5 was studied also by XPS in order to characterize its surface composition in bigger detail. Wide survey XPS spectra confirmed the presence of the expected element Bi whereas C and O come from adsorbates (H_2O, CO_2, etc.), or surfactants and partial surface oxidation (Figure S3). High-resolution Bi 4f XPS spectrum of Bi-S5 (Figure 6) revealed a degree of oxidation for the surface layers of Bi NPs. Bi 4f region is divided into two well-separated spin-orbit components ($4f_{7/2}$ and $4f_{5/2}$) with a separation of 5.3 eV. Bi 4f region was deconvoluted into zerovalent bismuth Bi^0 and its oxide (Bi^{III}) at 157 and 159 eV, respectively.[42-44] The peak corresponding to Bi^0 has an asymmetric shape but the oxide peak is symmetric. The fitting of those peaks suggests a Bi^0/Bi_2O_3 ratio of 72/28 % being present onto the particles outer layer. This result is not surprising since Bi is known to have a certain propensity for oxidation, though less pronounced compared to other pnictogen elements such as Sb and As. In fact, the XPS results shown herein are not contradictory to the XRD measurements of the sample under discussion: XPS is a surface-sensitive technique, studying only the outer ~ 10 nm layer of the particles, which is indeed more prone to oxidation than the overall volume of the nanostructures. In addition, XRD cannot detect any non-crystalline oxide entities, which will be however be identified by XPS.

HRTEM imaging of the sample Bi-S5 shows that the hexagonal nanoplates are composed of different crystalline domains. In certain zones, the crystal plane interval of 0.32 nm can be found, assigned to the (012) lattice plane of rhombohedral Bi (Figure S4b), in agreement with the XRD. The respective SAED pattern consists of clearly observed spots (inset of Figure S4b), indicating a good crystallinity and high quality fot the produced structures. No diffuse or broad ring patterns are observed, rendering the presence of any amorphous phases as unlikely. Still, the presence of surface oxide layers cannot be excluded, as implied by the above-mentioned XPS measurements.

In sample Bi-S6 all reagents were kept unchanged as in Bi-S5, but the heating conditions were turned back to 'moderate' ones (160 ^oC, 7h) as it was the case for the samples Bi-S1 – Bi-S4. Higher reaction temperatures are sometimes associated with better particle crystallinities. However, in the present work, all different samples, including those produced at intermediate temperatures, showed very good crystallinity as judged by their XRD measurements. Therefore we decided to test the moderate heating conditions also in Bi-S6, aiming to better control the particles morphology.

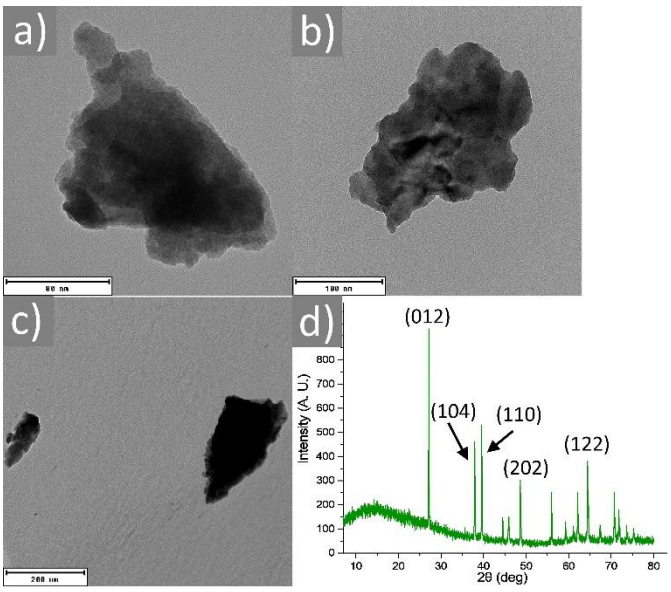

Figure 4. TEM images (a-c) and XRD measurement (d) for sample Bi-S4.

How particles grow can be controlled by both thermodynamic and kinetic factors. Adjusting the contribution of those types of factors is a way to modify the resulting particles morphology.[45] In general, higher reaction temperatures lead to thermodynamic-dominant growth modes, whereas moderate temperatures favour kinetic growth. The latter type of growth can result, under certain circumstances, to slowly growing anisotropic structures. On the other hand, a thermodynamic-based growth mode may lead to more spherical (and smaller in size) nanostructures. Figures 7a-c depict the presence of nanosheet-like bismuth flakes with sizes of a few hundreds of nanometers. Smaller nanoparticles with ill-defined shape and a tendency to agglomerate are also spotted in the TEM grid. The above demonstrate that even if heating conditions may affect the final particle size and shape, the combination of precursors, solvents, surfactants and reducing agents is still of paramount importance for the determination of the final nanostructure morphology. Once again, it is noted that a given mixture of surfactant-reductant-solvent may be excellent for the controlled synthesis and stabilization of a nanomaterial with a certain composition, but it may perform moderately when the aim is monodisperse size and homogeneous morphology for a nanomaterial composed of a different element. The affinity of the different reagents with the produced material may vary, thus causing dissimilar growth modes and resulting morphologies.

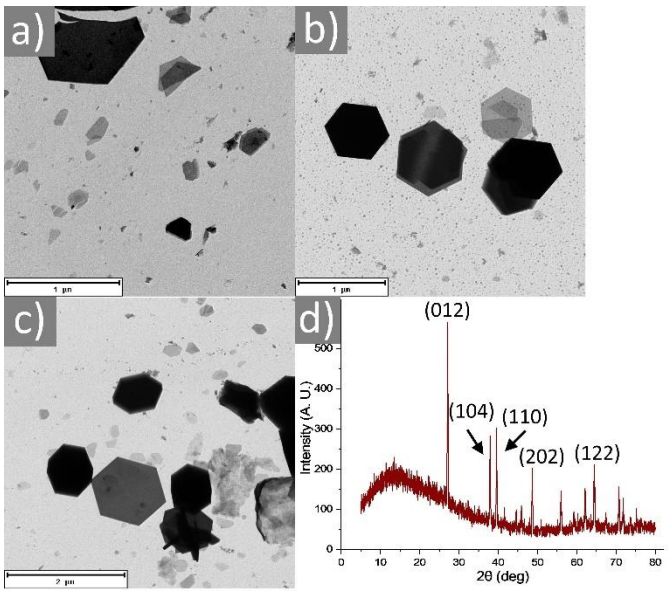

Figure 5. TEM images (a-c) and XRD measurement (d) for Bi-S5.

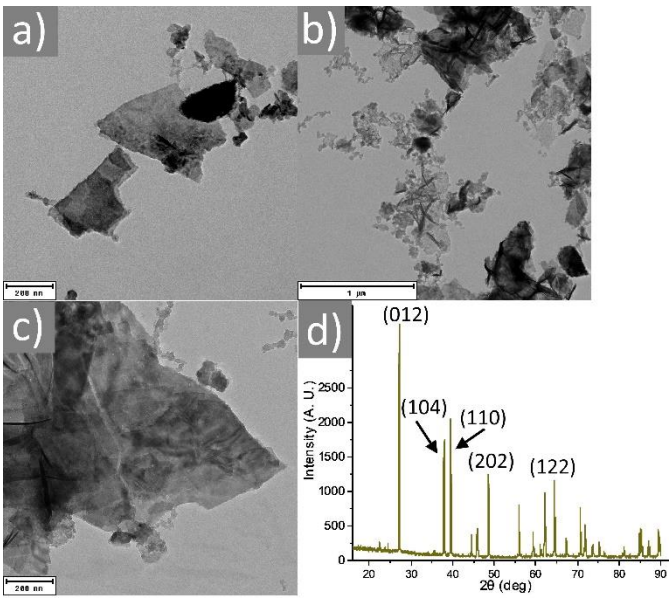

Figure 7. TEM images (a-c) and XRD measurement (d) for sample Bi-S6.

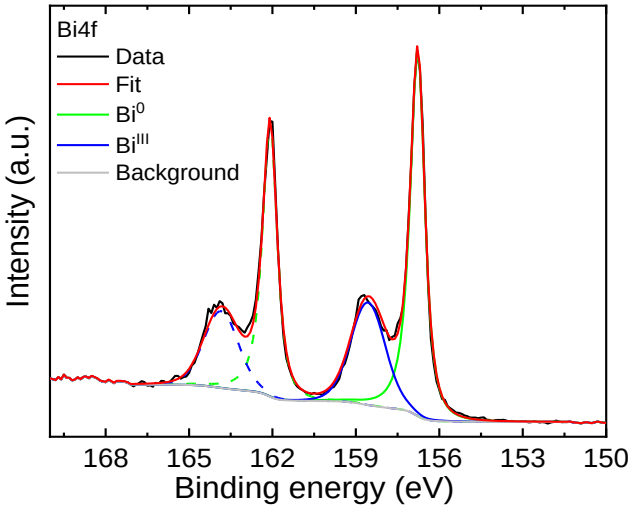

Figure 6. High-resolution XPS spectrum of Bi 4f for the sample Bi-S5. The solid and dashed lines represent Bi $4f_{7/2}$ and Bi $4f_{5/2}$ components respectively.

Electrocatalytic properties of Bi nanostructures towards the NRR

The catalytic activity of Bi nanostructures in the NRR was studied and compared between different morphologies using a two-compartment cell with a proton-exchange membrane as the separator. Firstly, inherent electrochemistry was characterized to study the electrochemical stability concerning different morphologies and sizes of the synthesized Bi NPs. A CV was recorded between 0.2 and -2 V vs. sat. Ag/AgCl in 0.1 M KOH (pH = 13) where two pairs of redox peaks were noticed for almost all prepared materials (Figures S5-10). Oxidation occurred at *ca*. -0.5 V and subsequent reduction took place at -1 V vs. sat. Ag/AgCl. These peaks can be assigned to the redox pair Bi^0/Bi^{III} that has standard redox potential around -0.4 V vs. SHE (ca. -0.6 V vs. sat. Ag/AgCl). A subsequent oxidation to Bi^V is very unlikely to happen since the standard redox potential is more than 1 V higher compared to the Bi^0/Bi^{III} redox pair based on the following reactions:[46]

$2Bi^0 + 6OH^- \rightarrow Bi^{III}_2O_3 + 3H_2O + 6e^-$ -0.45 V vs. SHE

$Bi^0 + 3OH^- \rightarrow Bi^{III}OOH + H_2O + 3e^-$ -0.46 V vs. SHE

$Bi^0 + 3OH^- \rightarrow Bi^{III}(OH)_3 + 3e^-$ -0.38 V vs. SHE

$Bi^{III}_2O_3 + 3H_2O + 6OH^- \rightarrow 2Bi^V(OH)_6^- + 4e^-$ 0.80 V vs. SHE

$Bi^{III}OOH + H_2O + 3OH^- \rightarrow Bi^V(OH)_6^- + 2e^-$ 0.80 V vs. SHE

$Bi^{III}(OH)_3 + 3OH^- \rightarrow Bi^V(OH)_6^- + 2e^-$ 0.70 V vs. SHE

Therefore, such a reaction would occur at far more positive potential than the upper vertex used to record the CV. Based on previous reports on various nanomaterials, inherent redox behaviour can be influenced by the size of NPs where the oxidation potential decreases as the particle size increases.[47-49] Moreover, the crystal plane orientation can play a significant role as well, *e.g.* edge and basal plane of layered materials can have dramatically different

electrochemical behaviour than nanostructures of more conventional shapes, such as nearly spherical ones.[50] In summary, all of the observed differences in the inherent electrochemistry behavior of the different samples should be caused by their distinct shapes.

The NRR activity of sample Bi-S1 was evaluated in the same electrolyte in an H-cell at potentials between –1.7 and –1.85 V. The highest ammonia yield was observed at – 1.8V, as demonstrated in Table 1, producing 157 ± 0.1 μgh^{-1}cm^{-2} corresponding to a Faradaic efficiency of 1.84 ± 0.2 %. Aiming for the best possible precision and reliability of the data derived, three independent measurements were recorded each time with a clean GC electrode under the same conditions. On the other hand, applying the potential of -1.7 V led to a FE of 3.29 ± 0.2 %, with the expense of a slightly lower NH_3 yield of 142 ± 0.1 μgh^{-1}cm^{-2}. More detailed results are shown in Table 1 and at the graphical representation of Figure 8.

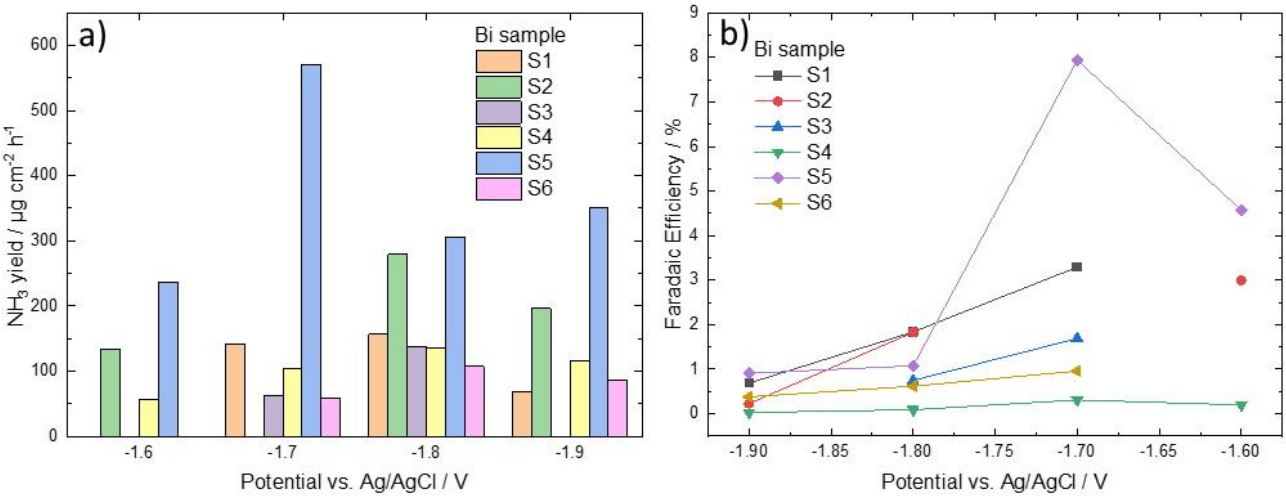

Figure 8. a) Ammonia formation rates and b) corresponding Faradaic efficiencies for the produced samples at different potentials.

The performance of sample Bi-S2 in what concerns FE was quite similar to that of Bi-S1. In particular, the highest FE for Bi-S2 was observed at a potential of -1.6 V (FE: 2.99%). Using a -1.8 V potential was associated with a quite higher ammonia yield for Bi-S2: 279 ± 0.1 μgh^{-1}cm^{-2}. The sample Bi-S3 demonstrated a decent level of NH_3 yield at -1.8 V: 142 ± 0.1 μgh^{-1}cm^{-2}. Still, its Faradaic efficiency showed a rather moderate value, being up to 1.69 ± 0.2 % for an applied potential of -1.7 V. Regarding the sample Bi-S4, its overall performance was worse in comparison to the above-mentioned sample. Though a considerable ammonia yield of 136 ± 0.1 μgh^{-1}cm^{-2} was obtained with an applied potential of -1.8 V, its highest FE was limited to 0.31 ± 0.2 %, using a potential of -1.7 V. A much improved catalytic activity was noted for the sample Bi-S5. More specifically, applying a -1.7 V potential resulted in a NH_3 yield at 571 ± 0.1 μgh^{-1}cm^{-2} with a respective FE at 7.94 ± 0.2 %. All these results are summarized in Table 1 and at the schematic view of Figures 8 and 9.

The stability of sample Bi-S5 toward the NRR was evaluated by a long-term overnight experiment (15 h) where the potential was kept at –1.7 V. This potential was chosen for the stability test since the N_2 reduction performance of Bi-S5 was optimized when applying that potential. There was no substantial decline of current density, as recorded during the 15 h interval as shown in Figure 10. No significant deterioration in ammonia yield or FE values was observed after such prolonged electrocatalytic duration. They were measured at 494 ± 0.1 μgh^{-1}cm^{-2} and 7.12 ± 0.2 % correspondingly. TEM images of the Bi NPs after long-term NRR catalysis demonstrated that the original morphology of the Bi nanostructures was preserved, showing the high stability of these nanostructures for NRR (Figure S11). In situ Raman measurements during the NRR process did not show any notable changes in the composition of the bismuth nanostructures during the 2h-reaction (Figure S13).

Apart from NH_3, the possible presence of hydrazine (N_2H_4) was also investigated at the otherwise same tested potentials for NH_3: only trace quantities of hydrazine were detected (maximum N_2H_4 yield at –1.7 V: 0.571 μgh^{-1}cm^{-2}). Hydrazine is a potential by-product of electrochemical ammonia synthesis. The above result illustrated that the Bi nanostructures of sample Bi-S5 possess a high degree of selectivity for electrochemical synthesis of NH_3. Though remarkable, the NRR performance of sample Bi-S5 is not that surprising: as the standard redox potential of N_2 reduction is more negative than that of the hydrogen evolution reaction (HER), the competitive HER is an important barrier for N_2 reduction. As the HER needs a more negative potential than NRR, overcoming HER competitiveness is a big challenge. More specifically, bismuth is a less reactive element that promotes the selectivity of N_2 activating without modifying the binding energy of further intermediates. Bi-based catalysts have several advantages, such as unique structure to capture and activate N_2 and low adsorption energy of H_2, so they may form an effective platform in the N_2-reduction field. The semi-conducting Bi is less reactive in the HER because of the high free energy barrier of adsorption of H_2 on the surface of Bi. The strong interaction between the Bi 6p band and the N 2p orbitals allows N_2 to be selectively adsorbed on its surface, which facilitates the dissociation of N≡N. Moreover, Bi atoms in Bi-based catalysts can localize the density

state near the Fermi level, which means that Bi atoms can offer more active centers for activating N_2 by donating p-electrons. At the same time, Bi can reduce the free-energy change in the potential-determining step. The aforementioned factors affect positively the NRR activity. In addition, the surface electron accessibility for the HER can be prevented as it has poor H_2 adsorption energy. Based on the above features, Bi-based materials indeed exhibit great potential in ammonia production under ambient conditions.[51]

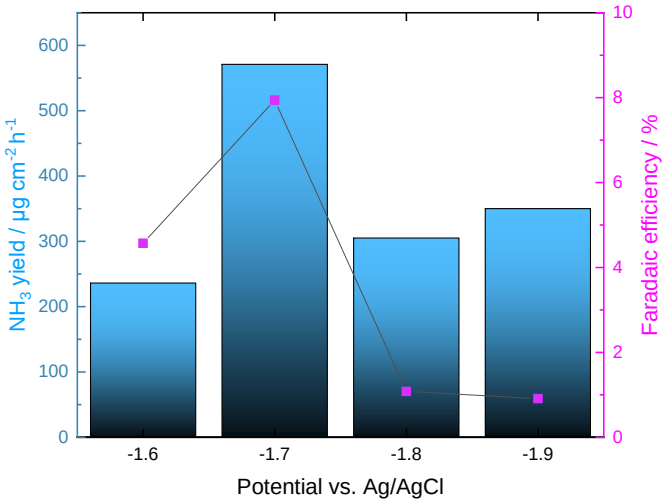

Figure 9. NH_3 formation rate and FE for the best NRR-performing sample, Bi-S5, at a range of potentials.

Finally, the overall performance of sample Bi-S6 can be deemed as rather moderate, with an ammonia yield of 107 ± 0.1 $\mu g h^{-1} cm^{-2}$ at -1.75 V and a maximum FE of 0.96 ± 0.2 % at -1.7 V. The ameliorated NRR performance of sample Bi-S5 in comparison to the rest samples can be mainly assigned to its thin 2D hexagonal-plate morphology, as shown by AFM: this endows a high surface area with numerous active sites such as edges and corners, which are easily accessed by the reagents. The enhanced possibility for the reagent molecules to collide with the active site favors a quite good NRR activity.[52] Apparently the surface oxidation of Bi nanoplates did not affect the electrocatalytic performance of Bi-S5 in a significant extent. In fact, also other 2D morphologies such as Bi nanosheets are known to provide more intrinsic energetic edge sites than Bi NPs, facilitating the adsorption and activation of N_2 molecules.[53] The presence of some small spherical NPs in Bi-S5 may also help toward the acquisition of high surface area and a bigger population of active sites for NRR. NRR active sites are the three-phase reaction interface, including N_2 (gas), protons (liquid) and electrons (solid). Electrochemical nitrogen reduction ($N_2 + 6H^+ + 6e^- \rightarrow 2NH_3$) is achieved by capturing N_2 followed by subsequent reduction steps, each of them involving one proton and one electron. A great number of active sites will help to capture and dissociate the dinitrogen more easily.[27]

Chronoamperometry tests were performed at different potentials aiming to study the catalytic activity and determine the optimal potential for the NRR. It seems that the choice of the applied potential was also a crucial point, since when more negative potentials were applied, the NH_3 yield and Faradaic efficiency were significantly decreased. The onset potential for electrochemical reaction is -0.18 V (vs. RHE), which has to do with the hydrogen evolution reaction (HER). When using Bi-based materials as the working electrode, the onset potential can shift to more negative values. This occurs probably thanks to the fact that Bi NPs can suppress the HER, at least to some extent.[27] Still, in the current work, when the selected potential was more negative for the different samples (*e.g.* -1.9 V, see Table 3), the decreased NH_3 yield and FE for the NRR might be attributed to the competitive selectivity toward the HER.[54] In fact it has been reported that in some cases the NH_3 yield can even increase but with a simultaneous decline for the FE, because of competition between HER and NRR.[55]

Besides high stability, activity, selectivity and a good degree of HER suppression, an ideal electrocatalyst for N_2 reduction should be able to achieve a remarkably high FE for the production of NH_3.[56] Compared to the measurements shown for the other samples of the current study, *i.e.* samples Bi S1-4 and Bi-S6, the sample Bi-S5 displayed higher ammonia yield and much higher Faradaic efficiency in varying potential conditions. Apart from its aforementioned morphological characteristics, the improved catalytic activity of sample Bi-S5 can be partly attributed also to the use of PEI as surfactant and growth modifier. In the case of ethanol oxidation reaction (EOR), we have previously shown that using PEI does not perturb the catalytic properties of metal and bimetallic nanostructures,[31,32] which is in agreement with the results obtained for Bi-S5 in the current work. It seems that somehow the cationic PEI allows a high NRR activity, at least under certain circumstances (that is, potentials applied and nanostructure morphologies). On the other hand, the anionic PSS (samples Bi-S1 and Bi-S2) was possibly attached more tightly onto the surface of the Bi structures, negatively affecting the reagents accessibility on the catalytic sites.

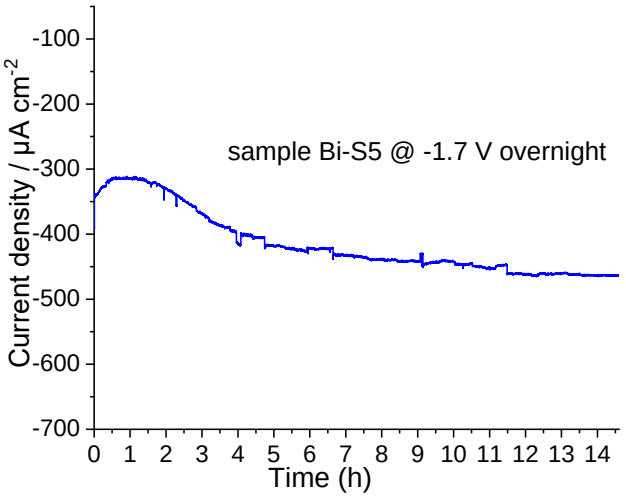

Figure 10. Long-term chronoamperometry measurement for the sample Bi-S5 recorded overnight, implying a good degree of compositional stability.

The electrocatalytic properties of sample Bi-S5 was comparable with several NRR electrocatalysts published up to date. For a good number of cases, the above-mentioned sample outperformed state-

of-the-art NRR electrocatalysts reported at ambient conditions. For instance, Au nanostructures have been reported to display lower NRR activity and selectivity than Bi ones, since bismuth is deemed to be a HER poisoner and has weaker tendency for the HER compared to gold.[57] Faradaic efficiencies ranging from 0.03% to 66% have been derived for the broad range of nanostructured materials, electrolytes and cell configurations rested for NRR.[58] However, for the majority of the electrochemical systems, despite catalyst type, Faradaic efficiencies are commonly under 1%.[59] Porous Ni catalysts provided a FE of 0.89% in a 2-propanol/water medium, whereas higher FE up to 8.11% was observed in gold nanoclusters of sub-nanometer dimension.[60] Tetrahexahedral (THH) Au nanorods yielded a FE of up to 4% at room temperature when used as NRR catalysts.[61] Wang and co-workers reported the use of N,P co-doped hierarchical porous carbon (NPC) for electrochemical NRR in an acid aqueous medium under ambient conditions. An ammonia yield up to 0.97 $\mu gh^{-1}mg^{-1}_{cat}$ with a FE up to 4.2% were obtained.[62]

Bi is a Group-VA element, and its stable valence-electronic structure does not inherently favor N_2 adsorption and activation. It has been proposed that the presence of defects might be responsible for the transformation of an almost non-catalytic though earth-abundant NRR material to a robust and active catalyst. Defect-rich Bi(111) nanoplates displayed a high FE of 11.68% with an ammonia production rate of 5.45 $\mu gh^{-1}mg^{-1}_{cat}$.[63] Bi@C catalysts annealed at 900 °C demonstrated a NH_3 yield rate up to 4.22 ± 0.33 $\mu gh^{-1}mg^{-1}_{cat}$ with a remarkable Faradaic efficiency of 15.10 ± 0.43%.[64] Bismuth nanosheets prepared by the *in situ* electrocatalytic topotactic transformation of BiOI nanosheets provided a NH_3 yield of 12.49 $\mu gh^{-1}mg^{-1}_{cat}$ with a respective FE of 7.09%. In that work, density functional theory (DFT) calculations demonstrated that despite the fact that the basal plane of the bismuth sheets was relatively inert, the exposed edge sites were suitable for the adsorption and activation of nitrogen molecules.[53] Qiao and co-workers presented the fabrication of 2D-mosaic Bi nanosheets by an *in situ* electrochemical reduction process. An ammonia yield of 2.54 $\mu gh^{-1}cm^{-2}$ with a corresponding FE of 10.46% were achieved. The sufficient exposure of edge sites coupled with effective p-orbital electron delocalization was considered as beneficial for such high NRR performance. On the other hand, more isotropic Bi NPs in that work provided a NH_3 yield of 0.268 $\mu gh^{-1}cm^{-2}$ with a Faradaic efficiency not exceeding the value of 0.66%.[2]

In another report, nanorod-like bismuth-based metal-organic frameworks (MOFs) were reduced *in situ* and fragmented into densely contacted Bi(0) NPs. The resulting particles displayed an excellent NRR activity in both neutral and acidic electrolytes, with a maximum NH_3 yield of 3.25 $\mu gh^{-1}cm^{-2}$, a FE of 12.11% and a very good selectivity for the formation of NH_3 rather than N_2H_4.[11] Other works on Bi nanostructures have reported the following values for ammonia yield and Faradaic efficiency: NH_3: 25.85 $\mu gh^{-1}mg^{-1}_{cat}$, FE: 10.8% (Bi nanodendrites),[54] NH_3: 23.4 $\mu gh^{-1}mg^{-1}_{cat}$ and FE 19.8% (Bi hollow spheres),[52]and NH_3 yield: 5.68 $\mu gh^{-1}cm^{-2}$ with a FE of 6.3% (Bi NPs on Ni foam).[27]

Table 1. NH_3 and N_2H_4 yields and the respective Faradaic efficiencies derived at different potentials for the Bi samples of this study (ammonia yield: green colour – FE: black colour with units: $\mu gh^{-1}cm^{-2}$ and % correspondingly).

	-1.6 V	**-1.7 V**	**-1.8 V**	**-1.9 V**
Sample Bi-S1		142/3.29	157/1.84	68/0.69
Sample Bi-S2	134/2.99		279/1.83	196/0.23
Sample Bi-S3		63/1.69	138/0.75	
Sample Bi-S4	56/0.2	104/0.31	136/0.09	115/0.03
Sample Bi-S5	236/4.57	571/7.94	305/1.08	350/0.91
Sample Bi-S6		59/0.96	107/0.62	86/0.38

Conclusions

To summarize, bismuth nanostructures of different shapes were produced by the solvothermal approach in an autoclave in the presence of surfactants. A range of reaction temperatures, solvents and stabilizers was investigated aiming to isolate the Bi structures with the most suitable morphology for nitrogen reduction reaction activity. It was found that large hexagonal two-dimensional bismuthene nanoplates with edges and tips in their morphology performed remarkably in the NRR with an ammonia yield 571 ± 0.1 $\mu gh^{-1}cm^{-2}$ with a respective FE at 7.94 ± 0.2 % at a potential of -1.7 V vs. sat. Ag/AgCl, with high selectivity against the production of hydrazine and good stability. Other morphologies displayed weaker NRR activity. Therefore we have confirmed that bismuth is capable

to catalyse nitrogen to ammonia reduction but the performance deeply relies on morphology and thickness of the resulting nanostructures.

Our work shows that simple colloidal chemical routes are convenient for the production of Bi nanostructures which are suitable for the NRR which is an eco-friendly reaction but with challenges to overcome such as sluggish kinetics and low selectivity.[65] Future objectives will be to adapt our synthetic protocol for bimetallic nanostructures such as Pd-Bi which have also been shown to be promising for the NRR.[66] The use of ionic liquids as electrolytes in an attempt to further increase the resulting FE will also be investigated.[67]

Table 2. Comparison of the performance of the sample Bi-S5 with other NRR electrocatalysts having Bi-based or different composition.

Material	Electrolyte	NH_3 yield	Faradaic efficiency (%)	Reference
Bi-S5 sample	0.1 M KOH	571 $\mu g h^{-1} cm^{-2}$	7.94	This work
Bi(111) nanoplates	0.2 M Na_2SO_4	5.45 $\mu g h^{-1} mg^{-1}_{cat}$	11.68	63
Bi@C	0.1 M Na_2SO_4	4.22 $\mu g h^{-1} mg^{-1}_{cat}$	15.1	64
Bi nanosheets	0.1 M $NaHCO_3$	12.49 $\mu g h^{-1} mg^{-1}_{cat}$	7.09	53
2D-mosaic Bi nanosheets	0.1 M Na_2SO_4	2.54 $\mu g h^{-1} cm^{-2}$	10.46	2
Isotropic Bi nanoparticles	0.1 M Na_2SO_4	0.268 $\mu g h^{-1} cm^{-2}$	0.66	2
Bi-based MOFs	0.1 M Na_2SO_4	3.25 $\mu g h^{-1} cm^{-2}$	12.11	11
Bi nanodendrites	0.1 M HCl	25.85 $\mu g h^{-1} mg^{-1}_{cat}$	10.8	54
Bi hollow spheres	0.1 M Na_2SO_4	23.4 $\mu g h^{-1} mg^{-1}_{cat}$	19.8	52
Bi NPs on Ni foam	0.5 M K_2SO_4	5.68 $\mu g h^{-1} cm^{-2}$	6.3	27
Nanoscale γ-Fe_2O_3	0.5 M KOH	12.5 $mol.h^{-1} mg^{-1}_{cat}$	1.9	5
Zr^{4+}-doped anatase TiO_2	0.1 M KOH	8.9 $\mu g h^{-1} cm^{-2}$	17.3	6
Porous Ni	10 mM H_2SO_4	$1.9*10^{-11}$ mol $s^{-1} cm^{-2}$	0.89	60
Sub-nanometer Au nanoclusters	0.1 M HCl	21.4 $\mu g h^{-1} mg^{-1}_{cat}$	8.11	60
Tetrahexahedral Au nanorods	0.1 M KOH	1.648 $\mu g h^{-1} cm^{-2}$	4	61
N,P-doped hierarch. porous C	0.1 M HCl	0.97 $mol.h^{-1} mg^{-1}_{cat}$	4.2	62

Conflicts of interest

There are no conflicts to declare.

Experimental

Materials

Bismuth nitrate pentahydrate (Fluka, 98% and Lachema 98%) were used as Bi sources. Diethyleneglycol (DEG, 99%) and branched polyethyleneimine (Mw ~ 25,000, 99%) were bought by Sigma-Aldrich, Czech Republic. Poly (sodium 4-styrene sulfonate) (PSS) was provided by Sigma-Aldrich, whereas hydrazine hydrate (50%) was bought by Penta. Dimethyformamide (DMF, GR) was bought from Lach:Ner.

Bismuth nanostructures were prepared using a range of different hydrothermal and solvothermal protocols. Table 3 summarizes the synthetic conditions followed for all samples. A more analytical description of the synthetic routes followed is below:

The preparation of **sample Bi-S1** was inspired from the literature.[22] Briefly, 2.94 g PSS and 2.5 g of hydrazine hydrate were added in 50 ml of distilled and deionized water. After that, 3.6 g of bismuth nitrate pentahydrate (Lachema, CZ) was dissolved in the above mixture. Vigorous stirring was applied for 30 min in a sealed beaker to produce a white milk-like colloidal suspension. The mixture was then transferred to a Teflon-lined stainless steel autoclave with a capacity of 120 ml and it was placed in a preheated oven at 160 °C

for 5 h. The autoclave was moved out of the oven after the 5 h heating interval and it was let to cool down naturally. The black precipitate was washed twice with excess water and then twice with excess ethanol at 3000 rpm for 30 min for each cycle. The product was dried overnight by being placed in a fume hood in ambient temperature. A mortar was used to grind the powders in order to obtain a fine powder which was used for further characterizations and electrocatalytic application. The yield was 1.27 g of black powder for this sample.

Sample Bi-S2 was produced with a protocol inspired from the literature.[23] 420 mg of PSS and 0.4 ml of hydrazine hydrate (50% water solution) were added in 50 ml of distilled and deionized water. 360 mg of $Bi(NO_3)_3{\cdot}5H_2O$ (Fluka) were then inserted and the system was stirred for 30 min to obtain a white suspension. The mixture was transferred into a Teflon-lined SS autoclave with capacity of 120 ml. It was afterwards introduced in a preheated oven at 160 ^oC for 6h. The resulting products were washed as in the sample Sa-1, but a centrifugation speed of 10000 rpm was employed. 135 mg of solid powder were recovered after drying and grinding.

Sample Bi-S3 was produced by first dissolving 860 mg of branched PEI in 50 ml H_2O. Then 0.4 ml of hydrazine hydrate were added, followed by the insertion of 360 mg of bismuth nitrate (Lachema). Stirring for 30 min was applied and the mixture was added in an autoclave, as above. It was inserted in a preheated oven at 160 ^oC for 7h. Washing was done twice with excess ethanol and twice with acetone, at 8500 rpm for 30 min at each cycle. Drying process was the same as above.

For the preparation of **sample Bi-S4**, 860 mg of PEI were first added in 30 ml of DMF under stirring. Following this, 485 mg of Bi-nitrate (Lachema) were dissolved in the mixture, and then 1 g of hydrazine hydrate was also added. After stirring for 30 min at 700 rpm, the autoclave was introduced at a preheated oven at 160 ^oC and kept at this temperature for 7h. Washing 4 times with excess ethanol (8500 rpm, 15 min each cycle) was carried out after cooling, before drying.

Sample Bi-S5 was produced as described below: 860 mg PEI were added in 30 ml DEG in an autoclave under stirring. 1 g hydrazine was then inserted to the reaction mixture followed by 485 mg of Bi-nitrate pentahydrate (Fluka). The mixture was placed in a preheated oven at 240 ^oC and kept there for 1h. After natural cooling to room temperature, the particles were washed twice with ethanol at 8500 rpm for 20 min. Then they were washed with acetone with the same conditions. After drying, a mortar was used to obtain a fine powder of nanostructures.

The **sample Bi-S6** was prepared similarly to Bi-S5, but the heating conditions were 160 ^oC for 7h (instead of 240 ^oC for 1h).

Table 3. Chemical reagents, reaction temperatures and morphological features for the produced Bi nanostructures

Sample name	Bi precursor	Surfactants/ Reductants	Solvent	Temp./Time	Morphology
Bi-S1	$Bi(NO_3)_3.5H_2O$ (3.6 g)	PSS (2.94 g) / $N_2H_4.H_2O$ (2.5 g)	Water (50 ml)	160 ^oC / 5 h	Large 2D and 3D structures
Bi-S2	$Bi(NO_3)_3.5H_2O$ (360 mg)	PSS (420 mg)/ $N_2H_4.H_2O$ (0.4 ml)	Water (50 ml)	160 ^oC / 6 h	80-120 nm NPs
Bi-S3	$Bi(NO_3)_3.5H_2O$ (360 mg)	PEI (860 mg)/ $N_2H_4.H_2O$ (0.4 ml)	Water (50 ml)	160 ^oC / 7 h	Ill-defined <100 nm NPs
Bi-S4	$Bi(NO_3)_3.5H_2O$ (485 mg)	PEI (860 mg)/ $N_2H_4.H_2O$ (1 g)	DMF (30 ml)	160 ^oC / 7 h	Irregular-shaped NPs >100 nm
Bi-S5	$Bi(NO_3)_3.5H_2O$ (485 mg)	PEI (860 mg)/ $N_2H_4.H_2O$ (1 g)	DEG (30 ml)	240 ^oC / 1 h	2D nanosheets and NPs
Bi-S6	$Bi(NO_3)_3.5H_2O$ (485 mg)	PEI (860 mg)/ $N_2H_4.H_2O$ (1 g)	DEG (30 ml)	160 ^oC / 7 h	2D flakes of different sizes

Transmission electron microscopy images were acquired with a EFTEM JEOL 2200 FS microscope operating at an acceleration voltage of 200 kV. For TEM imaging, nanostructure dispersion was drop-casted on C-coated copper grids. The crystal structure of the NFs was studied with a Bruker D8 in Bragg-Brentano parafocusing geometry and applying Cu K_α radiation (λ=1.5418 Å). Diffraction patterns were recorded in the range from 2θ=20^o to 100^o. Samples for XRD were prepared by putting dry powders of the particles on a zero-background silicon wafer, which does not have any diffraction peaks at the measurement range. Raman spectra were obtained using an inVia Raman microscope (Renishaw, UK) in backscattering geometry equipped with a charge-coupled device detector and a DPSS laser (532 nm, 50 mW) with an applied power of 5 mW and 50x magnification objective. A small amount of material in the form of powder was put onto a piece of Si wafer. For in situ Raman measurements, a suspension of Bi nanostructures was drop-casted on a Au substrate. A special electrochemical cell was employed for that purpose (Figure S12), accompanied with Ag/AgCl as RE, a Pt wire as CE and a GC as WE with the material deposited onto the latter electrode surface. The cell was filled with KOH until the surface of the GC was entirely immersed and connected to an Autolab PGSTAT 204 (Metroohm, Switzerland) potentiostat. Throughout the NRR process, the cell was purged with dinitrogen gas and Raman spectra were recorded in 30 min intervals during which the applied laser power was increased to 50 mW. XPS measurements were carried out with an ESCAProbeP spectrometer (Omicron Nanotechnology Ltd., Germany) equipped with a monochromatic Al X-ray radiation source (1486 eV). Wide-scan investigations of all elements were performed

with subsequent high-resolution scans for bismuth (Bi 4f), carbon (C 1s) and oxygen (O 1s). Specimens for XPS study were placed on a conductive carbon tape. To eliminate the sample charging in the course of measurement, a low-energy e-gun was used (1-3 eV). All XPS spectra were then processed by CasaXPS software. Atomic force microscopy (AFM) observations were implemented using a Ntegra Spectra from NT-MDT. The surface scans were carried out in a tapping (semi-contact) mode. Cantilevers with a strain constant of 1.5 kN m^{-1} equipped with a standard Si tip with curvature radius lower than 10 nm were used for the measurements. The AFM imaging was performed by drop-casting a sample suspension (1 mg mL^{-1}) on freshly cleaved mica substrate. The measurement was carried out in ambient conditions with a scan rate of 1 Hz and scan line of 512. Data analysis was done using the software package Gwyddion.

Electrochemical experiments were carried out with an Autolab PGSTAT 204 (Metrohm, Switzerland) potentiostat. The glassy carbon electrode was first polished with an alumina suspension to renew the electrode surface and then washed and wiped before the electrochemical reactions. To modify the glassy carbon electrode, the clean electrode was coated with a 1.5 µL aliquot of the suspension of the material in question in acetonitrile and left to dry to create a layer of homogeneously dispersed material on the electrode surface. The original and modified glassy carbon electrodes were utilized as the working electrodes together with a potassium chloride-saturated Ag/AgCl reference electrode and a platinum counter electrode.
The setup used for NRR measurements is shown elsewhere.[68] The volume of the electrolyte (0.1 M KOH) in the anodic and cathodic chambers of the cell was 50 mL for each, and a 35 mL acid trap of 0.1 M H_2SO_4 was connected to both chambers. Both the anodic and the cathodic chambers were purged with high purity N_2 (99.999%) with a constant flow of 20 mL min^{-1} during the whole electrolysis process. Linear sweep voltammetry (LSV) was performed at a scan rate of 100 mV s^{-1}, to examine the potential window for NRR. Throughout all electrochemical measurements, a magnetic stirring at 600 rpm was applied and performed in room temperature (25 °C), and all potentials are referenced against the used KCl saturated Ag/AgCl electrode. The determination of ammonia and hydrazine produced in the course of the NRR was performed using a HI83300 multiparameter photometer (Hanna Instruments, Woonsocket, Rhode Island, USA) as explained in our previous work on BiTeI.[68]

Calculation of NH_3 and N_2H_4 Yield and Faradaic Efficiency

The ammonia formation rate was calculated according to equation (1): $NH_3(C_{NH3} \times V)/(MW_{NH3} \times Q)$ where CNH_3 is the measured NH_3 concentration after being corrected since the acid trap was diluted due to pH neutralization, V is the volume of either the cathode or the acid trap, t is the reduction reaction time, and A is the area of the electrode covered with Bi sample.
The Faradaic efficiency was calculated based on equation (2): $FE = (3F \times C_{NH3} \times V)/(Mw_{NH3} \times Q)$ where CNH_3 and V are as explained above, F is the Faraday constant, Mw_{NH3} is the molecular weight of ammonia (17 g mol^{-1}), and Q is the total charge of the electrode.

Supporting Information: additional CV scans, AFM and TEM images, HRTEM-SAED images, photograph of electrochemical cell for in-situ Raman measurements, Raman spectra, wide-survey XPS spectrum.

Acknowledgements

This work was supported by the ERC-CZ program (project LL2003) from the Ministry of Education Youth and Sports (MEYS).

Corresponding authors

Prof. Zdeněk Sofer – Department of Inorganic Chemistry, University of Chemistry and Technology Prague, Technická 5, 166 28, Prague 6, Czech Republic; orcid.org/0000-0002-1391-4448; e-mail: zdenek.sofer@vscht.cz

Dr. Stefanos Mourdikoudis – Department of Inorganic Chemistry, University of Chemistry and Technology Prague, Technická 5, 166 28, Prague 6, Czech Republic; orcid.org/0000-0001-7187-5128; e-mail: mourdikt@vscht.cz

Authors

Dr. Nikolas Antonatos – Department of Inorganic Chemistry, University of Chemistry and Technology Prague, Technická 5, 166 28, Prague 6, Czech Republic; orcid.org/0000-0003-2563-9970

Dr. Vlastimil Mazánek – Department of Inorganic Chemistry, University of Chemistry and Technology Prague, Technická 5, 166 28, Prague 6, Czech Republic; orcid.org/0000-0002-8524-3364

Mr. Ivo Marek – Central Laboratories, University of Chemistry and Technology Prague, 166 28 Prague 6, Czech Republic.

References

(1) Razzaque, S.; Khan, M. D.; Aamir, M.; Sohail, M.; Bhoyate, S.; Gupta, R. K.; Sher, M.; Akthar, J.; Revaprasadu, N. Selective synthesis of bismuth or bismuth selenide nanosheets from a metal organic precursor: investigation of their catalytic performance for water splitting. *Inorg. Chem.*, **2021**, *60*, 1449-1461.

(2) Li, L.; Tang, C.; Xia, B.; Jin, H.; Zheng, Y.; Qiao, S.-Z. Two-dimensional mosaic bismuth nanosheets for highly selective ambient electrocatalytic nitrogen reduction. *ACS Catal.,* **2019**, *9*, 2902-2908.

(3) Li, W.; Li, K.; Ye, Y.; Zhang, S.; Liu, Y.; Wang, G.; Liang, C.; Zhang, H.; Zhao, H. Efficient electrocatalytic nitrogen reduction to ammonia with aqueous silver nanodots. *Commun. Chem.,* **2021**, *4*, 10.

(4) Liu, J.; Ma, J.; Zhang, Z.; Qin. Y.; Wang, Y.-J.; Wang, Y.; Tan, R.; Duan, X.; Tian, T. Z.; Zhang, C. H.; Xie, W. W.; Li, N.-W.; Yu, L.; Yang, C.; Zhao, Y.; Zia, H.; Nosheen, F.; Zheng, G.; Gupta, S.; Wu X.; Wang, Z.; Qiu, J.; Zhou, G.; Xu, L.; Liu, K.; Fu, J.; Liu, M.; Choi, S.-I.; Xie, J.; Peng, X.; Li, T.; Lin, G.; Wang, J.; Han, J.; Liang, H.; Li, S.; Zhang, X.; Zhu, Y.; He, T.; Cui, X.; Wang, H.; Wei, Z.; Liu, Q.; Fan, G.; Liu, Q.; Sun. X.; Feng, Y.; Liu, Y.; Chu, K.; Qiu, Y.; Liu, X.; 2021 Roadmap: electrocatalysts for green catalytic processes. *J. Phys. Mater.*, **2021**, *4*, 022004.

(5) Kong, J.; Lim. A.; Yoon, C.; Jang, J. H.; Ham, H. C.; Han, J.; Nam, S.; Kim, D.; Sung, Y.-E.; Electrochemical synthesis of NH_3 at low temperature and atmospheric pressure using a γ-Fe_2O_3 catalyst. *ACS Sustain. Chem. Eng.*, **2017**, *5*, 10986.
(6) Cao, N.; Chen, Z.; Zang, K.; Xu, J.; Zhong, J.; Luo, J.; Xu, X.; Zheng, G. Doping strain induced bi-Ti^{3+} pairs for efficient N_2 activation and electrocatalytic fixation. *Nat. Commun.*, **2019**, *10*, 2877.
(7) He, Y.; Li, J.; Li, K.; Sun, M.; Yuan, C.; Chen, R.; Sheng, J.; Leng, G.; Dong, F.; Bi quantum dots implanted 2D C-doped BiOCl nanosheets: enhanced visible light photocatalysis efficiency and reaction pathway. *Chin. J. Catal.*, **2020**, *41*, 1430.
(8) Kumar, P.; Singh, J.; Pandey, A. C., Rational low temperature synthesis and structural investigations of ultrathin bismuth nanosheets. *RSC Adv.*, **2013**, *3*, 2313.
(9) Yang, F.; Elnabawy, A. O.; Schimmenti, R.; Song, P.; Wang, J.; Peng, Z.; Yao, S.; Deng, R.; Song, S.; Lin, Y.; Mavrikakis, M.; Xu, W. *Nature Commun.*, **2020**, *11*, 2088.
(10) Mourdikoudis, S.; Sofer, Z. Colloidal chemical bottom-up synthesis routes of pnictogen (As, Sb, Bi) nanostructures with tailored properties and applications: a summary of the state of the art and main insights. *CrystEngComm,* **2021**, *23*, 7876.
(11) Yao, D.; Tang, C.; Li, L.; Xia, B.; Vasileff, A.; Jin, H.; Zhang, Y.; Qiao, S.-Z.; In situ fragmented bismuth nanoparticles for electrocatalytic nitrogen reduction. *Adv. Energy Mater.*, **2020**, *10*, 2001289.
(12) Chen, Y.; Chen, D.; Chen, J.; Lu, Q.; Zhang, M.; Lu, B.; Wang, Q.; Wang, Z. Facile synthesis of Bi nanoparticle modified TiO_2 with enhanced visible light photocatalytic activity. *J. Alloys Compd.*, **2015**, *651*, 114.
(13) Lee, H. S.; Noh, J.-S.; Size-controlled bismuth nanoparticles physically grown by the support of cobalt atomic flux. *J. Cryst. Growth,* **2016**, *440*, 102.
(14) Bezerra. A. G. Jr.; Cavassin, P.; Machado, T. N.; Woiski, T. D.; Caetano, R.; Schreiner, W. H. Surface-enhanced Raman scattering using bismuth nanoparticles: a study with amino acids. *J. Nanopart. Res.*, **2017**, *19*, 362.
(15) Palanisamy, P.; Chavali, M.; Kumar, E. M.; Etika, K. C. Chapter 10 – Hybrid nanocomposites and their potential applications in the filed of nanosensors/gas and biosensors', pp. 253-280, In '*Nanofabrication for Smart Nanosensor Applications*', 2020, Elsevier.
(16) Senapati, S.; Maiti, P. Chapter 9 – Emerging bio-applications of two-dimensional nanoheterostructure materials, pp. 243-255, in *2D Nanoscale Heterostructured Materials* (Synthesis, Properties and Applications), Elsevier 2020.
(17) Li, A. D.; Liu, W. C.; Chapter 4 – Optical properties of ferroelectric nanocrystal/polymer composites, pp. 108-158 in *Physical Properties and Applications of Polymer Nanocomposites*, Woodhead Publishing Series in Composites Science and Engineering, 2010.
(18) Huang, G.; Lu, C.-H.; Yang, H.-H. Chapter 3 – Magnetic Nanomaterials for Magnetic Bioanalysis, pp. 89-109, in *Novel Nanomaterials for Biomedical, Environmental and Energy Applications*, Elsevier 2019.
(19) *Fundamentals and Supercapacitor Applications of 2D Materials*, ed. Rout, C. S.; Late, D. J. Elsevier 2021.
(20) Yon, M.; Marty, J.-D. Ciuculescu-Pradines, D. Chapter 6 – Amines and Amine-boranes' in the book '*Reducing Agents in Colloidal Nanoparticle Synthesis*', ed. Mourdikoudis, S. The Royal Society of Chemistry, 2021.
(21) Comesana-Hermo, M.; Sequestra, R.; Piquemal, J.-Y. Chapter 9 – Hydrides' in the book '*Reducing Agents in Colloidal Nanoparticle Synthesis*', ed. Mourdikoudis, S. The Royal Society of Chemistry, 2021.
(22) Ghazali, N. N.; Nor, N. M.; Razak, K. A.; Lockman, Z.; Hattori, T. Hydrothermal synthesis of bismuth nanosheets for modified APTES-functionalized screen-printed carbon electrode in lead and cadmium detection. *J. Nanopart. Res.*, **2020**, *22*, 211.
(23) Yang, H.; Li, J.; Lu, X.; Xi, G.; Yan, Y. Reliable synthesis of bismuth nanoparticles for heavy metal detection. *Mater. Res. Bull.*, **2013**, *48*, 4718.
(24) Jaji, N.-D.; Othman, M. B. H.; Lee, H. L.; Hussin, M. H.; Hui, D. One-pot solvothermal synthesis and characterization of highly stable nickel nanoparticles. *Nanotechnol. Rev.*, **2021**, *10***,** 318.
(25) Pananon, P.; Sriprachuabwong, C.; Wisitsoraat, A.; Chuysinuan, P.; Tuantranont, A.; Saparpakorn, P.; Dechtrirat, D. A facile one-pot green synthesis of gold nanoparticle-graphene-PEDOT:PSS nanocomposite for selective electrochemical detection of dopamine. *RSC Adv.,* **2018**, *8*, 12724.
(26) Chen, B.-W.; He. Y.-C.; Sung, S.-Y. Sung, Le, T. T. H.; Hsieh, C.-L.; Chen, J.-Y.; Wei, Z.-H.; Yao, D.-J. Synthesis and characterization of magnetic nanoparticles coated with polystyrene sulfonic acid for biomedical applications. *Sci. Technol. Adv. Mater.*, **2020**, *21*, 471.
(27) Li, G.; Pan, Z.; Lin, H.; An, L. In-situ formation of bismuth nanoparticles on nickel foam for ambient ammonia synthesis via electrocatalytic nitrogen reduction. *J. Alloys Compd.,* **2021**, *875*, 160006.
(28) Jeong, G. H.; Lee, Y. W.; Kim, M.; Han, S. W. Han. High-yield synthesis of multi-branched gold nanoparticles and their surface-enhanced Raman scattering properties. *J. Colloid. Interf. Sci*., **2009**, *329*, 97.
(29) Dehsari, H. S.; Ribeiro, A. H.; Ersoz, B.; Tremel, W.; Jakob, G. Asadi, K. Effect of precursor concentration on size evolution of iron oxide nanoparticles. *CrystEngComm*, **2017**, *19*, 6694.
(30) Khan, M. D.; Opallo, M.; Revaprasadu, N. Colloidal synthesis of metal chalcogenide nanomaterials from metal-organic precursors and capping ligand effect on electrocatalytic performance: progress, challenges and future perspectives. *Dalton Trans.*, **2021**, *50*, 11347.
(31) Mourdikoudis, S.; Montes-Garcia, V.; Rodal-Cedeira, S.; Winckelmans, N.; Perez-Juste, I.; Wu, H.; Bals, S.; Perez-Juste, J.; Pastoriza-Santos, I. Highly porous palladium nanodendrites: wet-chemical synthesis, electron tomography and catalytic activity. *Dalton Trans.,* **2019**, *48*, 3758.
(32) Mourdikoudis, S.; Chirea, M.; Zanaga, D.; Altantzis, T.; Mitrakas, M.; Bals, S.; Liz-Marzan, L. M.; Perez-Juste, J.; Pastoriza-Santos, I. Governing the morphology of Pt-Au heteronanocrystals with improved electrocatalytic performance. *Nanoscale,* **2015**, *7*, 8739.
(33) Yonezawa, T.; Zhu, S.; Nguyen, M. T. Chapter 15 – miscellaneous reductants' in the book '*Reducing Agents in Colloidal Nanoparticle Synthesis'*, ed. Mourdikoudis, S. The Royal Society of Chemistry, 2021.
(34) Heravi, M. M.; Ghavidel, M.; Mohammadkhani, L. Beyond a solvent: triple roles of dimethylformamide in organic chemistry. *RSC Adv.*, **2018**, *8*, 27832.
(35) Mourdikoudis, S.; Chirea, M.; Altantzis, T.; Pastoriza-Santos, I.; Perez-Juste, J.; Silva, F.; Bals, S.; Liz-Marzan, L. M. Dimethylformamide-mediated synthesis of water-soluble platinum nanodendrites for ethanol oxidation electrocatalysis. *Nanoscale*, **2013**, *5*, 4776.
(36) Mourdikoudis, S.; Altantzis, T.; Liz-Marzan. L. M.; Bals, S.; Pastoriza-Santos, I.; Perez-Juste, J. Hydrophilic Pt nanoflowers:

synthesis, crystallographic analysis and catalytic performance. *CrystEngComm*, **2016**, *18*, 3422.

(37) Antonoglou, O.; Dendrinou-Samara, C. Chapter 3 – Polyols as a toolbox for the preparation of inorganic-based nanostructures' in the book '*Reducing Agents in Colloidal Nanoparticle Synthesis'*, ed. Mourdikoudis, S.; The Royal Society of Chemistry, 2021.

(38) Arunkumar, P.; Jayajothi, C.; Jeyakumar, D.; Lakshminarasimhan, N. Structure-property relations in hexagonal and monoclinic $BiPO_4$:$Eu3^+$ nanoparticles synthesized by polyol-mediated method. *RSC Adv.*, **2012**, *2*, 1477.

(39) Vera-Robles, L. I.; Escobar-Alarcon, L.; Picquart, M.; Hernandez-Pozos, J. L.; Haro-Poniatowski, E., A biological approach for the synthesis of bismuth nanoparticles: using thiolated M13 phage as scaffold. *Langmuir*, **2016**, *32*, 3199.

(40) Li, Y.; Chen, J.; Shao, P.; Huang, J.; Peng, X.; Li, J.; Wang, G. Zhang, C.; Wen, Z., Molten-salt-assisted synthesis of bismuth nanosheets for long-term continuous electrocatalytic conversion of CO_2 to formate. *Angew. Chem. Int. Ed.*, **2020**, *59*, 20112.

(41) Yang, J.; Wang, X.; Qu, Y.; Wang, X.; Huo, H.; Fan, Q.; Wang, J.; Yang, L.-M.; Wu, Y. Bi-based metal-organic framework derived leafy bismuth nanosheets for carbon dioxide electroreduction. *Adv. Energy Mater.*, **2020**, *10*, 2001709.

(42) Yang. C.; Guo, C.; Guo, W.; Zhao, X.; Liu, S.; Han, X. Multifunctional bismuth nanoparticles as theranostic agent for PA/CT imaging and NIR laser-driven photothermal therapy. *ACS Appl. Nano Mater.*, **2018**, *1*, 820.

(43) Li, L.; Ma, D.-K.; Qi, F.; Chen, W.; Huang, S. Bi nanoparticles/Bi_2O_3 nanosheets with abundant grain boundaries for efficient electrocatalytic CO_2 reduction. *Electrochim. Acta*, **2019**, *298*, 580.

(44) Zhu, Q.; Cheng, M.; Yang, X.; Zhang, B.; Wan, Z.; Xiao, Q.; Yu, Y. Self-supported ultrathin bismuth nanosheets acquired by in situ topotactic transformation of BiOCl as a high performance aqueous anode material. *J. Mater. Chem. A*, **2019**, *7*, 6784.

(45) Ho, C.-H.; Chan, C.-H.; Huang, Y.-S.; Tien, L.-C.; Chao, L.-C. The study of optical band edge property of bismuth oxide nanowires α-Bi_2O_3. *Opt. Express*, **2013**, *21*, 11965.

(46) Bratch, S. G. Standard electrode potentials and temperature coefficients in water at 298.15 K. *J. Phys. Chem. Ref. Data*, **1989**, *18*, 1.

(47) Cao, P.; Wang, N.; Chen, D.; Sun, S.; Ma, H.; Lin, M.; Size-dependent optical and electrochemical properties of gold nanoparticles to L-cysteine. *Gold Bull.*, **2021**, *54*, 97.

(48) Hua, H.; Liu, Y.; Wang, D.; Li, Y. Size-dependent voltammetry at single silver nanoelectrodes. *Anal. Chem.*, **2018**, *90*, 9677.

(49) Kumar, A.; Buttry, D. A. Size-dependent anodic dissolution of water-soluble palladium nanoparticles. *J. Phys. Chem. C*, **2013**, *117*, 26783

(50) Marvan, P.; Huber, S.; Luxa, J.; Mazanek, V.; Sedmidubsky, D.; Sofer, Z.; Pumera, M. Edge vs. basal plane electrochemistry of layered pnictogens (As, Sb, Bi): does edge always offer faster electron transfer? *Appl. Mater. Today*, **2019**, *16*, 179.

(51) Hao, Q.; Liu, C.; Jia, G.; Wang, Y.; Arandiyan, H.; Wei, W.; Ni, B.-J. Ni, Catalytic reduction of nitrogen to produce ammonia by bismuth-based catalysts: state of the art and future prospects. *Mater. Horiz.*, **2020**, *7*, 1014.

(52) Wang, J.; Ren, Y.; Chen, M.; Cao, G.; Chen, Z.; Wang, P. Bismuth hollow nanospheres for efficient electrosynthesis of ammonia under ambient conditions. *J. Alloys Compd.*, **2020**, *830*, 154668.

(53) Xia, L.; Fu, W.; Zhuang, P.; Cao, Y.; Chee, M. O. L.; Dong, P.; Ye, M.; Shen, J. Engineering abudant edge sites of bismuth nanosheets toward superior ambient electrocatalytic nitrogen reduction via topotactic transformation. *ACS Sustainable Chem. Eng.*, **2020**, *8*, 2735.

(54) Wang, F.; Lv, X.; Zhu, X.; Du, J.; Lu, S.; Alshehri, A. A.; Alzahrani, K. A.; Zheng, B.; Sun, X. Bi nanodendrites for efficient electrocatalytic N_2 fixation to NH^3 under ambient conditions. *Chem. Commun.*, **2020**, *56*, 2107.

(55) Nazemi, N.; Panikkanvalappil, S. R.; El-Sayed, M. A. Enhancing the rate of electrochemical nitrogen reduction reaction for ammonia synthesis under ambient conditions using hollow gold nanocages. *Nano Energy*, **2018**, *49*, 316.

(56) Guo, X.; Gu, J.; Lin, S.; Zhang, S.; Chen, Z.; Huang, S. Tackling the activity and selectivity challenges of electrocatalysts toward the nitrogen reduction reaction via atomically dispersed biatom catalysts. *J. Am. Chem. Soc.*, **2020**, *142*, 5709.

(57) Hao, Y.-C.; Guo, Y.; Chen, L.-W.; Shu, M.; Wang, X.-Y.; Bu, T.-A.; Gao, W.-Y.; Zhang, N.; Su, X.; Feng, X.; Zhou, J.-W.; Wang, B.; Hu, C.-W.; Yin, A.-X.; Si, R.; Zhang, Y.-W.; Yan, C.-H. Promoting nitrogen electroreduction to ammonia with bismuth nanocrystals and potassium cations in water. *Nat. Catal.*, **2019**, *2*, 448.

(58) Tang, C.; Qiao, S.-Z. How to explore ambient electrocatalytic nitrogen reduction reliably and insightfully. *Chem. Soc. Rev.,* **2019**, *48*, 3166.

(59) Foster, S. L.; Perez Bakovic, S. I.; Duda, R. D.; Maheshwari, S.; Milton, R. D.; Minteer, S. D.; Janik, M. J.; Renner, J. N.; Greenlee, L. F. Catalysts for nitrogen reduction to ammonia. *Nat. Catal.,* **2018**, *1*, 490.

(60) Deng, J.; Iniguez, J. A.; Liu, C. Electrocatalytic nitrogen reduction at low temperature. *Joule,* **2018**, *2*, 846.

(61) Bao, D.; Zhang, Q.; Meng, F.-L.; Zhong, H.-X.; Shi, M.-M.; Zhang, Y.; Yan, J.-M.; Jiang, Q.; Zhang, X.-B. Electrochemical reduction of N_2 under ambient conditions for artificial N_2 fixation and renewable energy storage using N_2/NH_3 cycle. *Adv. Mater.,* **2017**, *29*, 1604799.

(62) Song, P.; Wang, H.; Kang, L.; Ran, B.; Song, H.; Wang, R.; Electrochemical nitrogen reduction to ammonia at ambient conditions on nitrogen and phosphorus co-doped porous carbon. *Chem. Commun.,* **2019**, *55*, 687.

(63) Wang, Y.; Shi, M.-m.; Bao, D.; Meng, F.-l.; Zhang, Q.; Zhou, Y.-t.; Liu, K.-h.; Zhang, Y.; Wang, J-z.; Chen, Z.-w.; Liu, D.-p.; Jiang, Z.; Luo, M.; Gu, L.; Zhang, Q.-h.; Cao, X.-z.; Yao, Y.; Shao, M.-h.; Zhang, Y.; Zhang, X.-B.; Chen, J. G.; Yan, J.-m.; Jiang, Q. Generating defect-rich bismuth for enhancing the rate of nitrogen electroreduction to ammonia. *Angew. Chem. Int. Ed.,* **2019**, *58*, 9464.

(64) Wan, Y.; Zhou, H.; Zheng, M.; Huang, Z.-H.; Kang, F.; Li, J.; Lv, R. Oxidation state modulation of bismuth for efficient electrocatalytic nitrogen reduction to ammonia. *Adv. Funct. Mater.,* **2021**, *31*, 2100300.

(65) Zhang, W.; Zhang, B.-W. Bi-atom electrocatalyst for electrochemical nitrogen reduction reactions. *Nano-Micro Lett.,* **2021**, *13*, 106.

(66) Wang, X.; Luo, M.; Lan, J.; Peng, M.; Tan, Y. Nanoporous intermetallic Pd_3Bi for efficient electrochemical nitrogen reduction. *Adv. Mater.,* **2021**, *33*, 2007733.

(67) Suryanto, B. H. R.; Du, H.-L.; Wang, D.; Chen, J.; Simonov, A. N.; MacFarlane, D. R. Challenges and prospects in the catalysis of electroreduction of nitrogen to ammonia. *Nat. Catal.,* **2019**, *2*, 290.

(68) Antonatos, N.; Kovalska, E.; Mazanek, V.; Vesely, M.; Sedmidubsky, D.; Wu, B.; Sofer, Z. Electrochemical exfoliation of

Janus-like BiTeI nanosheets for electrocatalytic nitrogen reduction. *ACS Appl. Nano Mater.,* **2021**, *4*, 590

ToC Figure

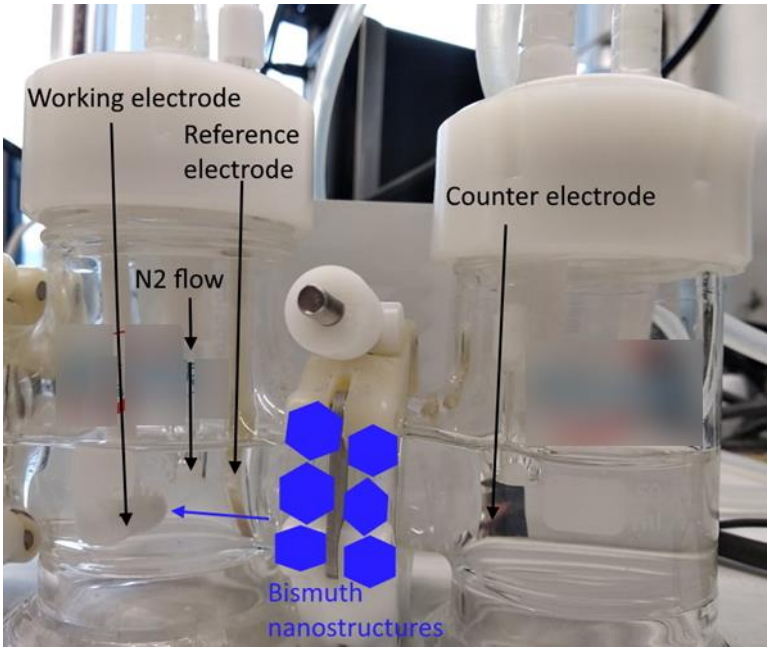

ToC synopsis: Bismuthene nanoplates as suitable agents for the electroreduction of dinitrogen. A constant N_2 flow ensures an inert atmosphere in the electrolyte cell throughout the reaction. The peculiar morphology of Bi nanostructures deposited onto the working electrode offers abundant active sites for the efficient reduction of N_2 to NH_3 with a competitive performance and stability